J. Fluid Mech. (2008), *vol.* 595, *pp.* 341–366.
doi:10.1017/S0022112007009251 Printed in the United Kingdom

The multi-mode stretched spiral vortex in homogeneous isotropic turbulence

KIYOSI HORIUTI AND TAKEHARU FUJISAWA

Department of Mechano-Aerospace Engineering, I1-64, Tokyo Institute of Technology, 2-12-1 O-okayama, Meguro-ku, Tokyo 152-8552, Japan
khoriuti@mes.titech.ac.jp

(Received 4 August 2006 and in revised form 20 September 2007)

The stretched spiral vortex is identified using direct numerical simulation (DNS) data for homogeneous isotropic turbulence and its properties are studied. Its genesis, growth and annihilation are elucidated, and its role in the generation of turbulence is shown. Aside from the two symmetric modes of configurations with regard to the vorticity alignment along two spiral sheets and the vortex tube in the core region studied in previous works, a third asymmetric mode is found. One of the two symmetric modes and the asymmetric mode are created not by a conventional rolling-up of a single vortex sheet but through the interaction among several sheets. The stagnation flow caused by the two sheets converges to form recirculating flow through its interaction with the vortex along the third sheet. This recirculating flow strains and stretches the sheets. The vortex tube is formed by axial straining, lowering of pressure and the intensification of the swirling motion in the recirculating region. As a result of the differential rotation induced by the tube and that self-induced by the sheet, the vortex sheets are entrained by the tube and form spiral turns. The transition between the three modes is examined. The initial configuration is in one of two symmetric modes, but it is transformed into another set of two modes due to the occurrence of reorientation in the vorticity direction along the stretched sheets. The symmetric mode tends to be more persistent than the asymmetric mode, among the two transformed modes. The tightening of the spiral turns of the spiral sheets produces a cascade of velocity fluctuations to smaller scales and generates a strongly intermittent dissipation field. To precisely capture the spiral turns, a grid resolution with at least $k_{\max}\overline{\eta} \approx 4.0$ ($k_{\max}$ is the largest wavenumber, $\overline{\eta}$ is the averaged Kolmogorov scale) is required. At a higher Reynolds number, self-similar spiral vortices are successively produced by the instability cascade along the stretched vortex sheets. A cluster consisting of spiral vortices with an extensive range of length scales is formed and this cluster induces an energy cascade.

1. Introduction

One of the characteristic features of turbulence is the generation of an energy cascade from large scales to small scales, and the subsequent energy dissipation that occurs in the smallest scale of turbulence (Kolmogorov scale). Another feature is the existence of organized vortical structures, termed ribbons, blobs, and worms (e.g. Jiménez & Wray 1998 and references therein). It may be expected that these two features are dependent, and certain structures are responsible for the energy cascade and dissipation. The primary elements of vortical structures are a filamentary object

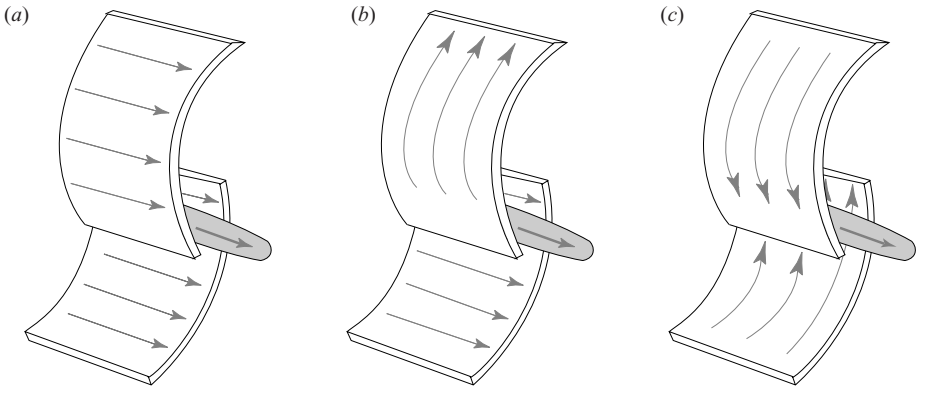

FIGURE 1. Schematics of three modes of vorticity vector alignment along a vortex tube and dual sheets. The grey arrows denote vorticity vectors. (*a*) Mode 1, (*b*) Mode 2, (*c*) Mode 3.

(the vortex tube) in which vorticity predominates the strain rate and a non-filamentary flat object (the vortex sheet) in which the strain rate and vorticity are comparably large and correlated (Horiuti 2001). The tube and sheet are related because the vortex tube is often formed by rolling-up of the vortex sheet, which is attributable to the focusing of vorticity via the Kelvin-Helmholz instability, e.g. see Kerr & Dold (1994) and Neu (1984).

Certain models have been considered to approximate vortical structures. Representative ones are the Burgers vortex tube model for a tube and the Burgers vortex layer model for a sheet (Burgers 1948). They are the exact steady solutions of the Navier–Stokes equation in which the inward convection and production of vorticity by stretching are balanced by outward diffusion. Lundgren (1982) introduced a model of generalized and non-axisymmetric Burgers vortices for the small-scale structure of turbulence. In this model, stretching by an axially symmetric strain and differential rotation of a vortex tube in the core region of the model causes vortex layers in the spiral to continually tighten (the Lundgren stretched spiral vortex, referred to hereafter as the LSV), and this mechanism causes an energy cascade. The LSV model gives the Kolmogorov $k^{-5/3}$ energy spectrum as the result of the axial stretching of a self-similar two-dimensional enstrophy cascade (Lundgren 1993). Gilbert (1993) provided a simplified cascade picture for the evolution of vorticity in the LSV; this spiral vortex was observed in bounded swirling flow with a rectangular planform (Lundgren & Mansour 1996). The spiral structure is the source of dissipation at the end of the cascade. This result is consistent with the observation using the direct numerical simulation (DNS) data that local dissipation is particularly strong, not within vortex tubes, but rather in their neighbourhood (e.g. Kerr 1985; Brachet *et al.* 1992; Reutsch & Maxey 1992; Vincent & Meneguzzi 1994).

A schematic of the configuration considered by Lundgren (1982) is shown in figure 1(*a*). In this model, the vorticity vectors or vortex lines along the vortex tube and the dual sheets surrounding the tube all point in the direction of the tube axis. This configuration is termed Mode 1. Pearson & Abernathy (1984), Moore (1985), and Kawahara, *et al.* (1997) considered the interaction of a diffusing line vortex and a linear shear flow with streamlines parallel to the line vortex. It was shown that the vortex lines wrap around the vortex tube with a swirling motion to form spiral layers of high transverse or azimuthal vorticity. The schematic of the configuration of the vorticity vectors in this model is shown in figure 1(*c*) (Mode 3).

In an analysis of the scaling properties of the LSV (Malik & Vassilicos 1996), it was shown that however small the amplitude of the velocity field self-induced by the spiral sheet, the effects of the spiral sheet on the frequency spectra cannot be overlooked. Pullin & Lundgren (2001) considered the spectral properties of the LSV model with non-axial vorticity (Mode 3), and showed that this model induces a $k^{-7/3}$ spectrum at large wavenumbers, and the energy dissipation incurred by the axial and azimuthal vorticities can be of comparable magnitudes. Kawahara (2005) showed that intense dissipation is generated along the spiral sheets in Mode 3, and that the contribution of spirals to the total dissipation dominates that of the tube. We note that mere topological classification yields an asymmetric mode, as shown in figure 1(*b*) (Mode 2).

In the LSV models cited above, a line vortex was embedded *a priori* as an initial condition of the flow, and it was allowed to diffuse under the action of viscosity. However, these models do not deal with the generation of a vortex tube in the core region. Reutsch & Maxey (1992) studied the temporal evolution of small-scale vorticity and passive scalar structures. It was shown that the vortex tube is formed by rolling-up of the vortex sheet through Kelvin-Helmholtz instability and that the scalar gradient sheets are generated through the interaction of antiparallel vortex regions; however, no spiral structures were observed as in the later study by Vincent & Meneguzzi (1994).

The rolling-up of the vortex sheet and the concentration of the axial vorticity yield the LSV with the Mode 1 configuration. This simplistic scenario, however, would not lead to the generation of the LSV in Modes 2 and 3, whereas the existence of Mode 2 or 3 LSV was reported in homogeneous isotropic turbulence (Kida & Miura 2000). We consider that it is important to assess the existence of LSVs because they may play vital roles in a turbulence cascade. The aim of this study is to extract LSVs and analyse their complete creation in homogeneous isotropic turbulence. Then, we explore the implications of the appearance of LSVs for turbulence energy cascade and dissipation in § 2. Two representative examples of Mode 1 and Mode 2 LSVs are presented. The transition between the three modes of LSVs and the roles of the LSV in the generation of energy cascade and dissipation are discussed. In § 3, the effect of grid resolution on the characterization of fine scales of an LSV is shown. In § 4, the effects of Reynolds number on the LSV creation and turbulence cascade are studied. Our conclusions are given in § 5.

2. Formation of LSVs

2.1. *Description of DNS data*

In this section, we give the details of the DNS data used for our assessment. They are in incompressible and homogeneous isotropic turbulence and decay in time. In table 1, the computational parameters are summarized. Periodic boundary conditions are imposed in the x-, y-, and z-directions. The size of the computational domain is 2π in each direction. The Fourier pseudospectral method is used, and aliasing errors are removed using the 3/2-rule. Time integration is carried out using a third-order Runge–Kutta scheme. The initial velocities are provided as random fields with the energy spectrum function $E(k)$ specified for Runs 1–3 as

$$E(k) = \frac{256}{35}\frac{\sqrt{2}}{\pi}k_p^{-1}\left(\frac{k}{k_p}\right)^8 \exp\left\{-2\left(\frac{k}{k_p}\right)^2\right\}, \tag{2.1}$$

Run	N	ν	R_λ	$\langle K\rangle$	$\langle\varepsilon\rangle$	L	λ	$\overline{\eta}(\times10^{-3})$	$k_{\max}\overline{\eta}$
1	1024	0.00138	77.43	0.904	0.654	0.468	0.138	8.00	4.09
2	512	0.00138	76.87	0.897	0.654	0.469	0.137	8.00	2.05
3	256	0.00138	77.2	0.900	0.654	0.469	0.138	8.00	1.02
4	1024	0.00024	122.5	0.962	0.296	0.466	0.0887	2.63	1.35

TABLE 1. Parameters for the computed cases: number of grid points N; kinematic viscosity ν; Taylor-microscale Reynolds number R_λ; average kinetic energy $\langle K\rangle$; average dissipation rate $\langle\varepsilon\rangle$; integral length scale L; Taylor microscale λ; average Kolmogorov length $\overline{\eta}(=(\nu^3/\langle\varepsilon\rangle)^{1/4})$; grid resolution criterion ($k_{\max}$ is the maximum wavenumber).

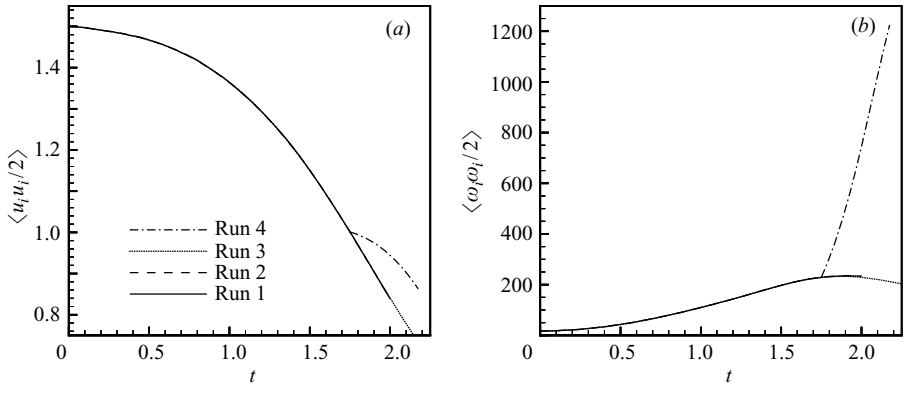

FIGURE 2. Temporal variations in (*a*) average turbulent energy ($K=\frac{1}{2}\langle u_i^2\rangle$) and (*b*) average enstrophy ($\frac{1}{2}\langle\omega_i^2\rangle$) obtained from Runs 1 to 4.

where $k_p=2$ (Chasnov 1991), and the r.m.s. value of initial velocity fluctuations, $u_0'=1.0$. The values of parameters for Runs 1–3 when the enstrophy is maximum ($t\approx1.925$) are given in table 1. The eddy turnover time $\tau_0\,(=L_0/u_0')=0.819$ for Runs 1–3, where L_0 is the integral length scale at $t=0$. In Run 4, the initial velocity field is provided from Run 1 at $t=1.75$, and the viscosity is decreased to $\nu=0.00024$. The parameters at $t=1.95$ are shown in table 1. Figures 2(*a*) and 2(*b*) show the temporal variations in turbulence kinetic energy and enstrophy, respectively.

Using Runs 1–3, we examine the dependence of turbulence statistics on grid resolution. Run 3 satisfies the conventional criterion for the resolution, $k_{\max}\overline{\eta}\approx1.0$, while Runs 2 and 1 do so for ≈2.0 and ≈4.0, respectively. Figure 3 shows the probability density function (p.d.f.) of the dissipation rate ε normalized by its average in the whole domain $\langle\varepsilon\rangle$. The large values exhibit marked differences although their average values are close to each other. The maximum values are 113.5, 105.7 and 66.63 for Runs 1, 2, 3, respectively. Run 3 does not capture the strong intermittency of ε. As is noted by Sreenivasan (2004), the DNS data based on the conventional criterion $k_{\max}\overline{\eta}\approx1.0$ are inadequate in representing the small-scale intermittency of dissipative structures. This point is discussed in detail in § 3. The insufficient resolution of Run 3 is also shown in the energy spectra (figure 4), which show a slight upturn in the highest-wavenumber region. Since the performance of Run 3 is critically poor, we utilize the DNS data from Runs 1 and 2 for assessment at a low Reynolds number.

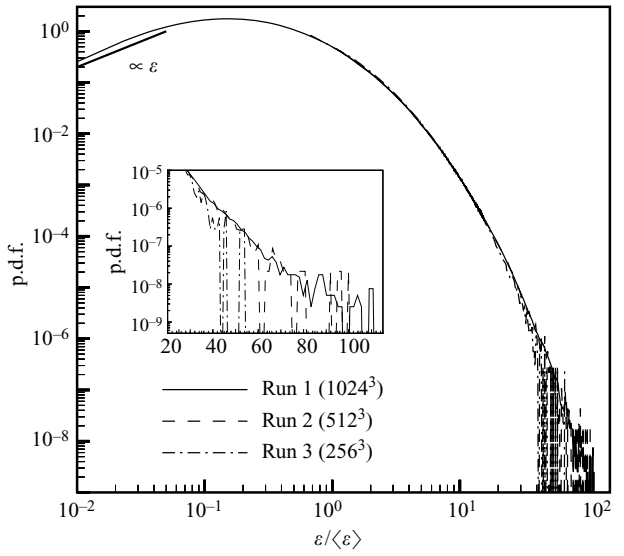

FIGURE 3. Distribution of the p.d.f. for the dissipation rate, $\varepsilon/\langle\varepsilon\rangle$, for Runs 1, 2, 3 at $t = 2.0$. $R_\lambda =$ 72.15, 72.14 and 74.02 for Runs 1, 2 and 3, respectively. The main figure shows the p.d.f. in log-log scales (plotted at every 2 bins), and the inset shows a log-linear plot (every 3 bins).

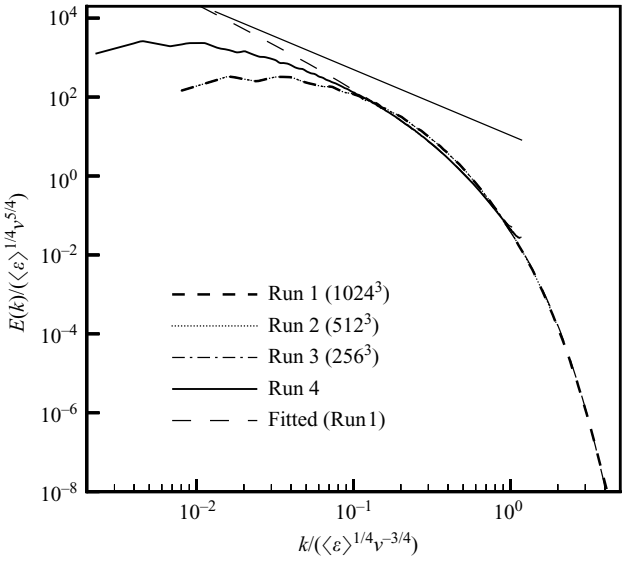

FIGURE 4. Normalized energy spectra obtained from Runs 1–3 at $t = 1.9$, and Run 4 at $t = 2.125$. $E(k)/(\langle\varepsilon\rangle\nu^5)^{1/4}$ is plotted versus $k\overline{\eta}$. The straight solid line indicates scaling with $k^{-5/3}$. The thin dashed line shows the approximation obtained using (3.1).

2.2. *Identification method for vortical structures*

In this study, reordering is applied to the eigenvalues of the second-order symmetric tensor, e.g., the eigenvalues of the strain-rate tensor $S_{ij}(= \frac{1}{2}(\partial u_i/\partial x_j + \partial u_j/\partial x_i))$, σ_i $(i = 1, 2, 3)$ are reordered as follows. When the eigenvector of S_{ij} is maximally aligned with the vorticity vector $\boldsymbol{\omega}$, the corresponding eigenvalue is chosen as

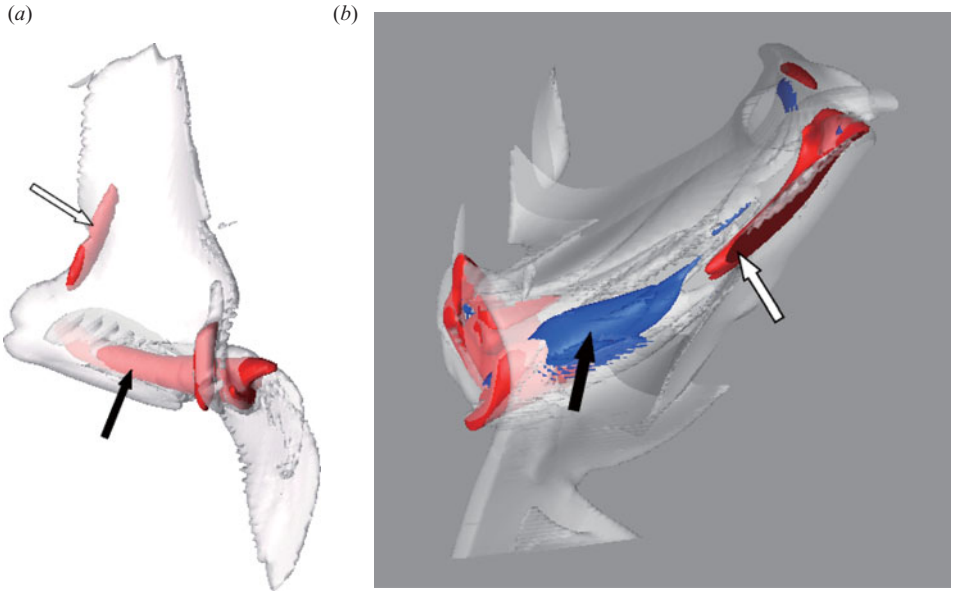

FIGURE 5. Three-dimensional rendering of the vortex sheets, tubes and $-S_{ij}\Pi_{ji}$. The sheets are identified using the isosurfaces of $[A_{ij}]_+$ (plotted using grey, $[A_{ij}]_+ = 1000$). (*a*) The tubes identified using Q (red, $Q = 1200$) at $t = 1.90$. (*b*) Isosurfaces of $-S_{ij}\Pi_{ji}$ obtained at $t = 1.95$ (red: $-S_{ij}\Pi_{ji} = 26000$; blue: -7000). Π_{ji} is the pressure Hessian defined in (2.4).

σ_s, the largest remaining eigenvalue as σ_+, and the smallest one as σ_-. The corresponding strain-rate eigenvectors are denoted $\boldsymbol{e}_s$, $\boldsymbol{e}_+$, $\boldsymbol{e}_-$ (Andreotti 1997; Horiuti 2001). The identification method for the vortical structures used in this study is as follows. For the vortex sheet, we use one of the eigenvalues of the tensor $A_{ij} = -(S_{ik}\Omega_{kj} + S_{jk}\Omega_{ki})$, to which the same reordering is applied. Ω_{ij} denotes the vorticity tensor, $\Omega_{ij} = \frac{1}{2}(\partial u_i/\partial x_j - \partial u_j/\partial x_i)$. We use one of the eigenvalues, $[A_{ij}]_+$ (Horiuti & Takagi 2005). For the vortex tube, we use the pressure p and also the second-order invariant of the velocity-gradient tensor, $Q(= -\frac{1}{2}(S_{ik}S_{ki} + \Omega_{ik}\Omega_{ki}))$, which is a source term for pressure. In the following section, we consider the variables and equations on the basis of $\boldsymbol{e}_s$, $\boldsymbol{e}_+$, $\boldsymbol{e}_-$, e.g., the vorticity components ω_s, ω_+, ω_- are $\omega_s = \boldsymbol{\omega}\cdot\boldsymbol{e}_s$, $\omega_+ = \boldsymbol{\omega}\cdot\boldsymbol{e}_+$, $\omega_- = \boldsymbol{\omega}\cdot\boldsymbol{e}_-$, respectively.

We classify the velocity vector field using the index number defined as

$$I(C) = I(R, \mathsf{x}_0) = \frac{1}{2\pi}\oint_C \mathrm{d}\zeta, \tag{2.2}$$

where integration is carried out in a counterclockwise direction along the circle C with its centre at $\mathsf{x}_0 = (x_0, y_0, z_0)$ and radius R. ζ denotes the angle that the velocity vector makes with the horizontal axis of the plane and $I(C)$ is the integration of the increment of ζ, $\mathrm{d}\zeta$, along C. $I(C)$ is an integer, and $I(C) = 1$ when C encloses circular or swirling flows, and $I(C) = -1$ when C encloses a stagnation flow, $I(C) = 0$ when C encloses a uniform flow.

We show the resulting visualization in figure 5(*a*), which is a three-dimensional rendering of the side view of the isosurfaces of $[A_{ij}]_+$ and Q at $t = 1.90$. In figure 5(*a*), the isosurfaces of $[A_{ij}]_+$ and Q are drawn using grey and red, respectively. Several vortex tubes, which are extracted as a concentrated region of Q, are shown in figure 5(*a*). The tube indicated by the white arrow is created by rolling-up of a single

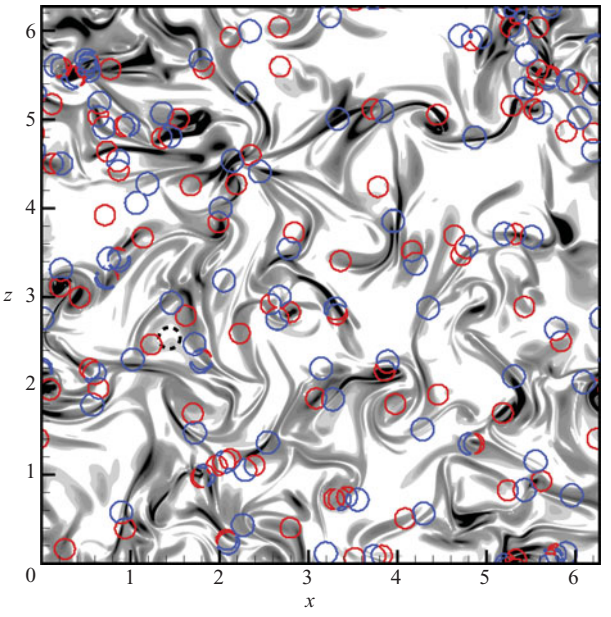

FIGURE 6. Distributions of $[A_{ij}]_+$ and the index number $I(C)$ in the (x, z) plane at $y = 0.17$ and $t = 1.20$. The contours of $[A_{ij}]_+$ are shown in grey scale [contour levels from 400 to 5200]. The red and blue circles indicate the boundaries of the regions in which $I(C) = 1$ and -1, respectively. The size of the plotted domain is $693\,\overline{\eta}$.

vortex sheet due to the Kelvin–Helmholz instability. The tube indicated by the black arrow (referred to as Example I in the following) is wrapped by spiralling vortex sheets, and its structure is similar to that of the LSV proposed by Lundgren (1982). Example I, however, is created not by rolling-up of a single vortex sheet but through the interaction of multiple sheets. In the following, we show the genesis, growth and annihilation stages of Example I. The entire process is organized into six stages. The DNS data obtained from Run 2 are used for the figures up to $t < 1.7$ because there is no noticeable difference between the results obtained from Runs 1 and 2. At $t \geqslant 1.7$, those obtained from Run 1 are used (see § 3).

2.3. *Genesis phase of LSV*

Figure 6 shows the distribution of vortex sheets at $t = 1.20$. The isocontours of $[A_{ij}]_+$ in the (x, z)-plane at $y = 0.17$ are shown. Note that the increments of contour levels for $[A_{ij}]_+$ are not uniform, and a smaller contour increment has been used for low and high levels rather than for intermediate levels. The lowest contour levels for $[A_{ij}]_+$ are in grey. Many vortex sheets are discernible. The LSV shown in figure 5 is created in the region indicated by the heavy dashed circle at $x \approx 1.4, z \approx 2.5$. In figure 6, the distribution of the index number $I(C)(= I(R, \boldsymbol{x}_0))$ is included, where the circle C is placed in the same (x, z)-plane. $I(C)$ is calculated at each grid point $\boldsymbol{x}_0$ and the circle is centred at $\boldsymbol{x}_0$ with $R = 0.2$ $(18.7\overline{\eta})$. $I(C) = -1$ on the grid points inside the blue circle; $I(C) = 1$ inside the red circle. In figure 6, many intertwined blue and red circles are discernible, which are generated when the swirling flow is near the stagnation flow and $R \geqslant l_s$ (l_s is the distance between the centre of the recirculating flow and the stagnation point). $I(C) = 0$ on the grid points outside the blue and red circles, including those in the region between the intertwined blue and red circles. The

regions with $I(C)=0$ can be divided into two groups by the variance of the angle increment $\mathrm{d}\zeta$ along C. In the non-vortical regions in which the flow is nearly uniform, the variance is small (<0.1 rad). The isocontours of the variance ($\geqslant 0.1$ rad) almost overlap with those of $[A_{ij}]_+$ (figure not shown), and the vortical regions including the intertwined regions can be characterized by large variance ($\gtrapprox 0.1$ rad). The fractions of the grid points at which $I(C)=1$ and $I(C)=-1$ are 0.056 and 0.057, respectively, and the fraction at which $I(C)=0$ and the variance $\geqslant 0.1$ rad is 0.48. Therefore, the stagnation, recirculation, intertwined flow and vortical sheet-like regions occupy $\approx 59\%$ of the entire region (Dávila & Vassilicos 2003). Because the velocity field and $I(C)$ are dependent on the frame of reference, it is more accurate to calculate them in the reference frame moving with the velocity at the point where the pressure is minimal in the recirculating region. However, it is difficult to accomplish this for all recirculating regions. We consider that the index number calculated in the fixed frame provides the overall characterization of the velocity field.

Figures 7–9 show schematics of the arrangement of the vortex sheets, the vorticity and velocity vectors at each stage and the DNS data corresponding to each schematic.

[i] Figure 7(a) shows a schematic of the arrangement of the vortex sheets and the velocity and vorticity vectors. The stagnation flow generated by the sheets marked S1 and S2 stretches S2. This stagnation flow converges by interacting with the sheet marked S3 and the vortex along S3, and recirculating flow is formed. Figure 7(b) is an enlargement of the recirculating region at an earlier time, indicated by the the heavy dashed circle in figure 6. It shows the isocontours of $[A_{ij}]_+$ and the distributions of velocity vectors projected onto the (x, z)-plane at $y=0.17$ and $t=1.125$ corresponding to figure 7(a). An arrangement of two sheets similar to S1 and S2 shown in figures 7(a) and 7(b) is shown in figure 4 of Herring & Kerr (1993).

[ii] As is shown in figure 7(c), S2 and S3 are strained and stretched by the recirculating flow and the swirling flow caused by the vortex along S3. Figure 7(d) shows the corresponding isocontours of $[A_{ij}]_+$ and p at $t=1.150$. The vortex sheets marked by black arrows in figure 7(d) are stretched in the directions indicated by the arrows by the recirculating and swirling flows.

[iii] As shown in figure 8(a), S2 and S3 are further strained and stretched by the recirculating and swirling flows. Figure 8(b) shows the corresponding isocontours of $[A_{ij}]_+$ and p at $t=1.200$. Two sheets, namely, the lower and upper sheets, marked L and U, respectively, are formed.

[iv] As shown is in figure 8(c), the portions of the stretched S2 and S3, marked L and U are detached. Figure 8(d) shows the corresponding isocontours of $[A_{ij}]_+$ and p at $t=1.500$. It can be seen that the low-pressure region is enclosed by the two sheets, L and U.

2.4. *Growth phase of LSV*

[v] As shown in figure 9(a), the low-pressure region in the recirculating flow is absorbed into the lower sheet (L). Figure 9(b) shows the corresponding isocontours of $[A_{ij}]_+$ and p at $t=1.750$. Note that the low-pressure region is absorbed into one of the two sheets (L) in which the vorticity vectors point in the same direction as in the low-pressure region.

Figure 10 shows the isocontours of $[A_{ij}]_+$, σ_s, and $\widetilde{\Pi}_{++}$ (see (2.6) below) at $t=1.750$. The region with $\sigma_s<0$ is discernible surrounding the low-pressure region indicated by the black arrow. The occurrence of compression in the s-direction, $\sigma_s<0$, is attributed primarily to a large positive pressure Hessian term, $\widetilde{\Pi}_{ss}$ (see (2.6)), in the same region (figure not shown). Another pressure Hessian term, $\widetilde{\Pi}_{++}$,

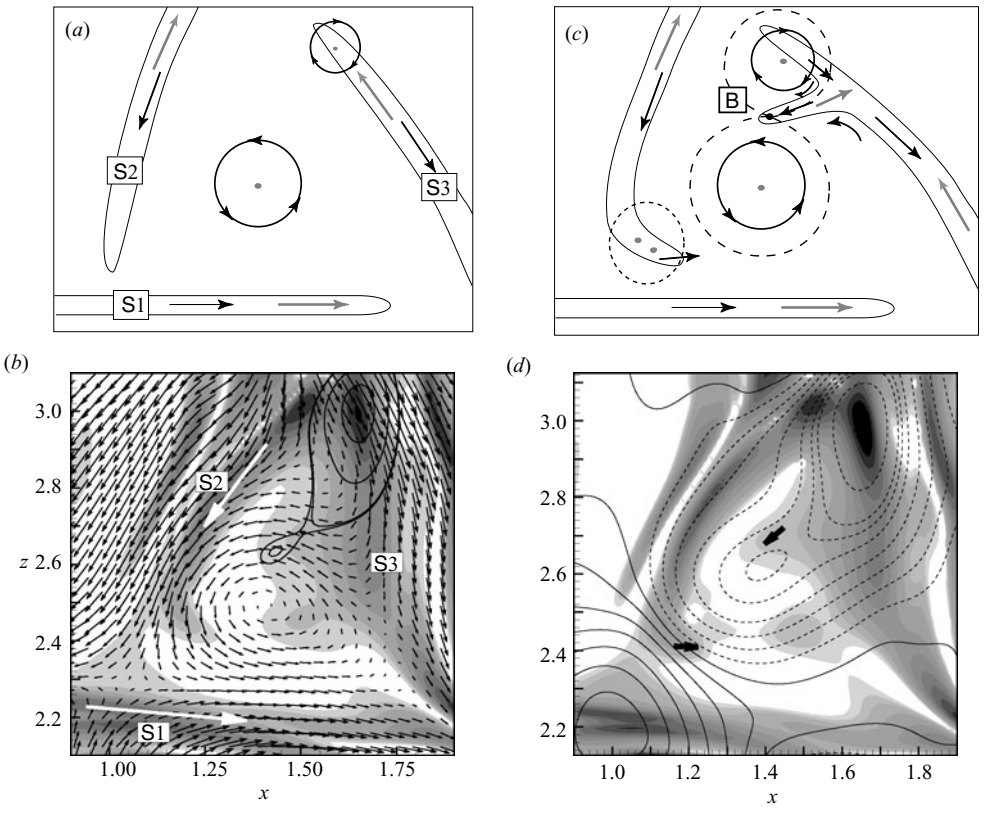

FIGURE 7. (*a*) Schematic of formation of stage [i]. S1, S2 and S3 are vortex sheets. The black arrows denote the velocity vectors, and the grey arrows the vorticity vectors. (*b*) Isocontours of $[A_{ij}]_+$ and velocity vectors in a cross-section of the (x, z)-plane at $y = 0.17$ at $t = 1.125$. Contours are shown in grey scale for $[A_{ij}]_+$ [from 40 to 320 (with increments of 40)], solid lines for p [−3.01 to −4.0 (0.5)], velocity vectors are plotted at every 4 grid points. The white arrows denote the directions of the velocity vectors on the sheets. (*c*) Schematic of stage [ii]. The long-dashed lines denote the isocontours of p. B is the saddle point of p. The region enclosed by the short-dashed line denotes the region in which a change in vorticity direction takes place. (*d*) Isocontours of $[A_{ij}]_+$ [40 to 360 (40)] and pressure p [−1.0 to 4.0] at $t = 1.15$. Positive values of p are plotted in solid lines, and negative ones in dashed lines.

reacts to relax the occurrence of this compression, as shown in figure 10. Because $\nabla^2 p = (\widetilde{\Pi}_{++} + \widetilde{\Pi}_{--} + \widetilde{\Pi}_{ss})$, $\nabla^2 p$ takes large positive values, and the pressure in the region indicated by the heavy dashed line is further lowered.

As shown in figure 9(*c*), the lowering of pressure intensifies the swirling motion, and the core region of the tube is formed. Axially straining fields induced by the vortices in near neighbours of the low-pressure region decreases the area of the cross-section of the tube and vorticity concentrates (Lundgren 1982). Figure 9(*d*) shows the isocontours of $[A_{ij}]_+$ and p at $t = 1.850$. The vorticity in the low-pressure region concentrates and grows, and the core region of the LSV is formed. Note that the recirculating flow stretches and entrains not only L and U, but also other sheets, e.g., S1 in figure 7(*b*) is stretched and placed near L in figure 9(*d*).

[vi] Figure 11 shows the isocontours of $[A_{ij}]_+$ and p at $t = 1.950$. The lower and upper sheets are further stretched and entrained by the tube, causing the sheets to

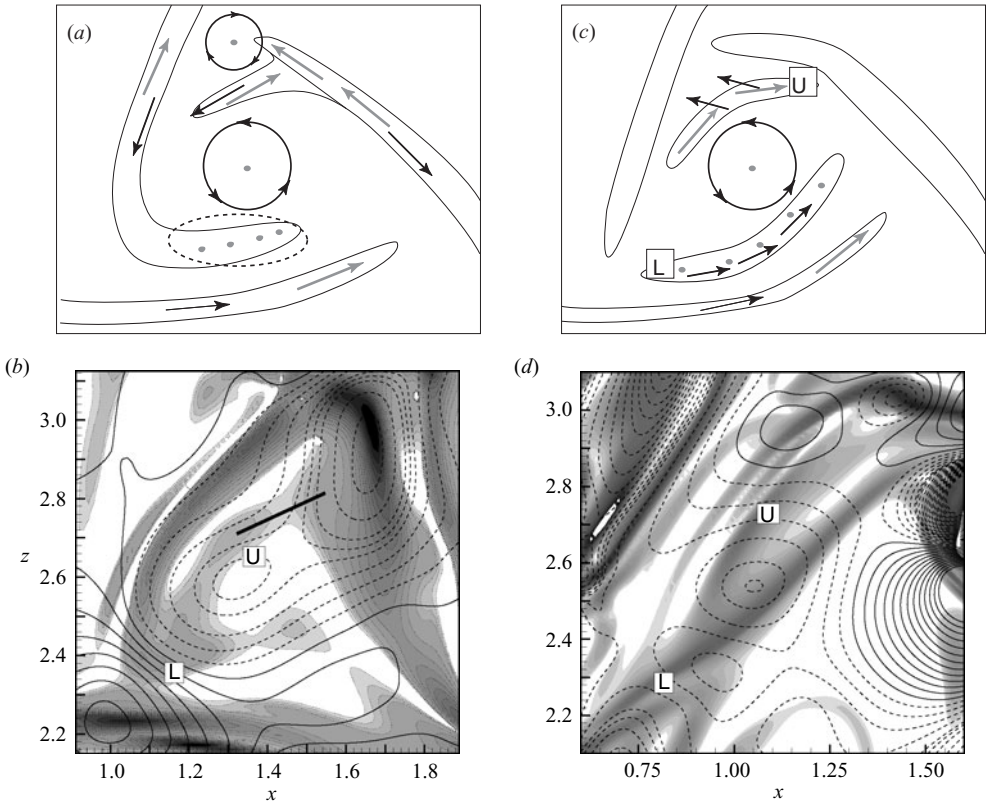

FIGURE 8. (*a*) Schematic of stage [iii]. The region enclosed by the dashed line denotes the region in which a change in vorticity direction takes place. (*b*) Isocontours of $[A_{ij}]_+$ [50 to 600] and p [−3.5 to 3.5] in a cross-section of the (x, z)-plane at $y = 0.17$ at $t = 1.2$. (*c*) Schematic of stage [iv]. (*d*) Isocontours of $[A_{ij}]_+$ [60 to 1400] and p [−3.5 to 3.0] at $t = 1.5$.

form a spiral. This spiral tightens and forms spiral turns. It is revealed that the LSV does indeed exist in homogeneous isotropic turbulence.

The formation of spiral turns is attributed to differential rotation. The strength of differential rotation can be evaluated as

$$D = r\frac{\partial}{\partial r}\left(\frac{u_\theta}{r}\right), \tag{2.3}$$

where r and θ are the radial and circumferential directions in polar coordinates around the tube axis, respectively, and u_θ is the θ-component of velocity (Gilbert 1993). Since the azimuthal length and thickness of a vorticity blob with an initial length of l_0 become $l_0 D\,T$ and $l_0/(D\,T)$, respectively, after the time T (Gilbert 1993), the vortex sheet is further stretched and becomes very thin when D is large. Figure 12 shows the distribution of D. We detected the axis of the vortex tube (Kida & Miura 1998), and the contours in figure 12 are shown in the (x_1, x_2)-plane perpendicular to the tube axis located at $x \approx 0.88$, $z \approx 2.47$ in figure 9(*d*). It can be seen that D takes larger values along the sheets than in the tube core region shown by the heavy dashed line. This result indicates that the vortex sheets self-induce a large u_θ and differential rotation.

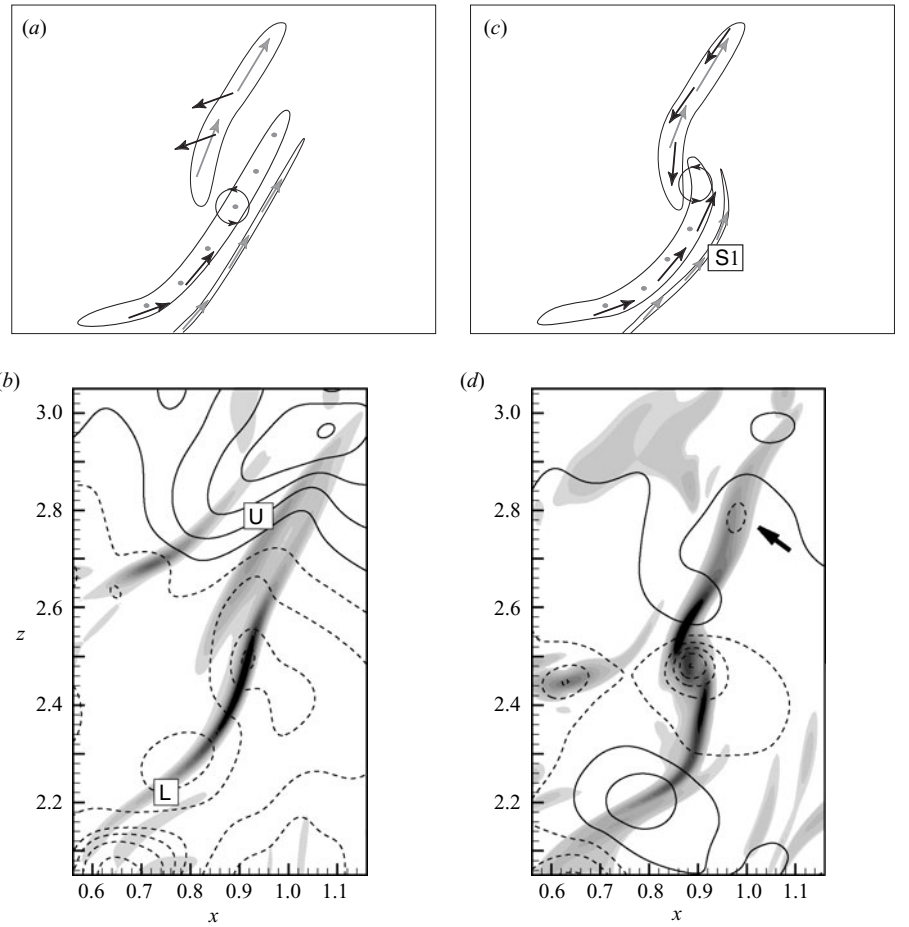

FIGURE 9. (*a*) Schematic of stage [v]. (*b*) Isocontours of $[A_{ij}]_+$ [400 to 4400] and p [−2.5 to 2.0] in a cross-section of the (x, z)-plane at $y = 0.27$ at $t = 1.75$. (*c*) Schematic of stage [vi]. (*d*) Isocontours of $[A_{ij}]_+$ [300 to 4400] and p [−5.0 to 2.0] at $t = 1.85$.

Figures 13(*a*) and 13(*b*) show the distributions of dissipation rate normalized by $\langle\varepsilon\rangle$, and $P(\equiv -S_{ik}S_{kj}S_{ji} + \Omega_{ik}\Omega_{kj}S_{ji})$, respectively. The governing equations for $S_{ij}S_{ij}$ and $\Omega_{ij}\Omega_{ij}$ are

$$\frac{\mathrm{D}}{\mathrm{D}t}\left(\tfrac{1}{2}S_{ij}S_{ij}\right) = -S_{ik}S_{kj}S_{ji} - \Omega_{ik}\Omega_{kj}S_{ji} - S_{ij}\Pi_{ji}, \tag{2.4}$$

$$\frac{\mathrm{D}}{\mathrm{D}t}\left(\tfrac{1}{2}\Omega_{ij}\Omega_{ij}\right) = 2\Omega_{ik}\Omega_{kj}S_{ji}, \tag{2.5}$$

where $\Pi_{ij}(=\partial^2 p/\partial x_i \partial x_j)$ is the pressure Hessian term and the viscous terms are omitted. P is the summation of the production terms for $\frac{1}{2}S_{ij}S_{ji}$ and $\frac{1}{2}\Omega_{ij}\Omega_{ij}$, and is essentially the derivative skewness, considered to represent the strength of the energy cascade into small scales (Horiuti 2003). In figures 13(*a*) and 13(*b*), both ε and P take large values along the spiral sheets because strain rate and vorticity are simultaneously amplified along the sheet (Horiuti & Takagi 2005). The correlation

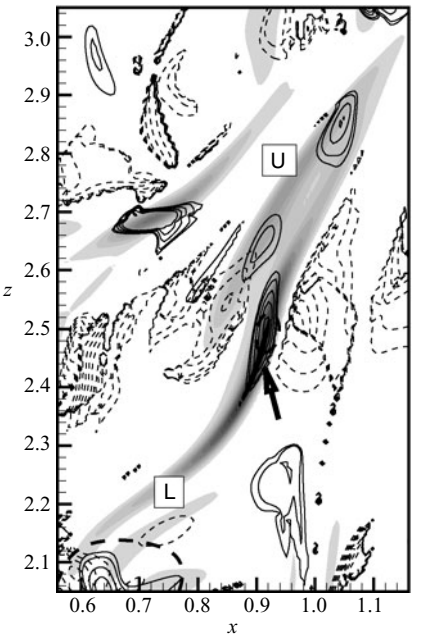

FIGURE 10. Isocontours of $[A_{ij}]_+$ (grey scale) in the (x, z)-plane at $y = 0.27$ and at $t = 1.750$ [400 to 4800] (Run 1). Dashed lines show the isocontours of σ_s [−10 to −1] and solid lines show the isocontours of $\widetilde{\Pi}_{++}$ [150 to 500]. The heavy dashed line shows the isocontour of p [−1.675].

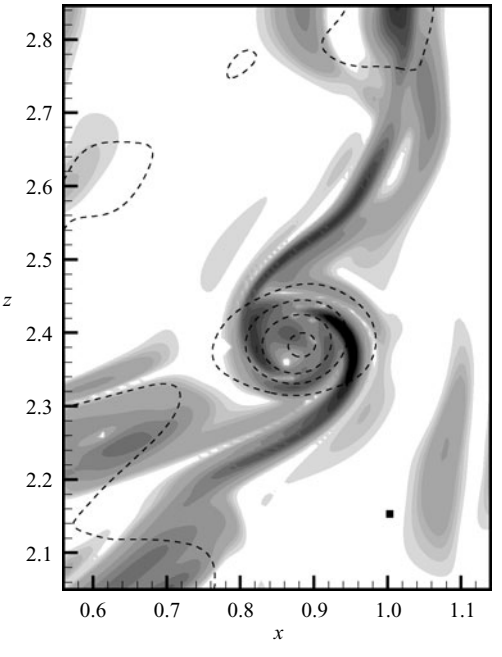

FIGURE 11. Isocontours of $[A_{ij}]_+$ (grey scale) [100 to 2250] and p [−7.0 to −1.0] in the (x, z)-plane at $y = 0.17$ and $t = 1.950$. The black square at $x = 1.0, y = 2.15$ represents the computational grid cell in (x, z)-plane. The sizes of the plotted domain are $72.5\overline{\eta}$ and $100\overline{\eta}$ in the x- and z-directions, respectively.

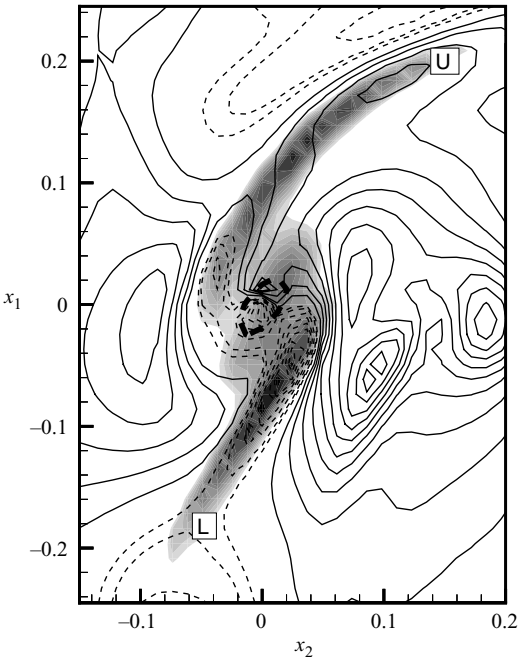

FIGURE 12. Isocontours of $[A_{ij}]_+$ (grey scale) [2500 to 5250] and D [−40 to 50 (5)] in the cross-section perpendicular to the tube axis at $t = 1.850$ (Run 2). Positive values are plotted by solid lines, and negative ones by dashed lines. Heavy dashed line is the isocontour of p [−4.7].

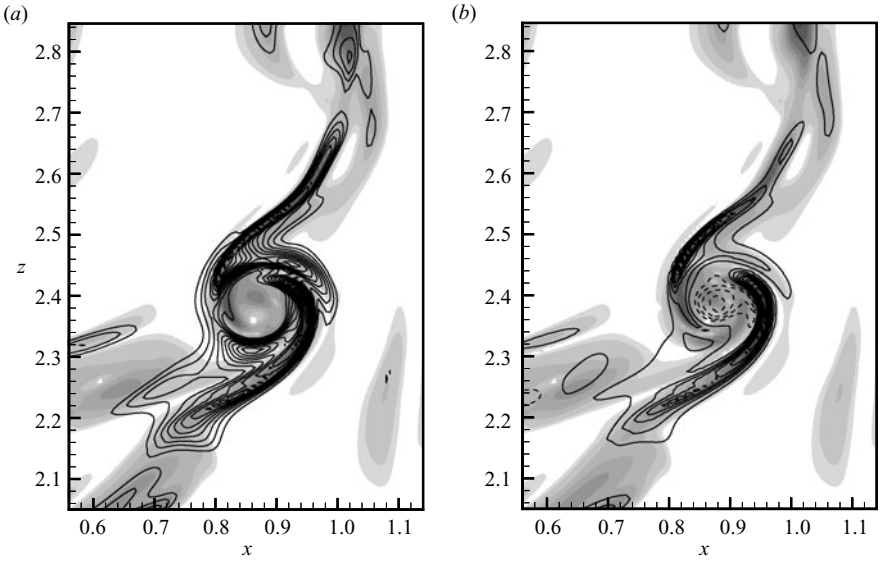

FIGURE 13. Isocontours of $[A_{ij}]_+$ (grey scale) [150 to 2750] and (*a*) $\varepsilon/\langle\varepsilon\rangle$ [3 to 15], (*b*) $-S_{ik}S_{kj}S_{ji} + \Omega_{ik}\Omega_{kj}S_{ji}$ [−2000 to 90000] in the (x, z)-plane at $y = 0.17$ and $t = 1.950$. Positive values are plotted by solid lines, and negative ones by dashed lines.

coefficient between ε and $[A_{ij}]_+$ is ≈ 0.79 at $t = 1.95$. Note that ε takes values up to 15 times its average value (Kawahara 2005). These are the results of the stretching and thinning of the sheet by differential rotation.

2.5. *Annihilation phase of LSV*

It can be seen in figure 13(*b*) that P becomes negative in the core region of the tube. This negativity is primarily attributed to $\Omega_{ik}\Omega_{kj}S_{ji} < 0$ and component-wise, $\sigma_s\omega_s^2 < 0$. Similarly, $\Omega_{ik}\Omega_{kj}S_{ji}$ is negative along the axis of the tube shown in figure 5(*a*) (figure not shown), and the vorticity diminishes in this region. This LSV is quickly annihilated with lapse of time and the spiral turns fade (Ruetsh & Maxey 1992). As the vorticity in the core region increases with the axial stretching of the LSV, $\Omega_{ik}\Omega_{kj}S_{ji}$ increases in stages [5] and [6], and in turn this causes a decrease in strain rate according to (2.4) (Rosales & Meneveau 2006 and references therein). As a result, σ_s and $\sigma_s\omega_s^2$ become negative in the region where $\Omega_{ik}\Omega_{kj}S_{ji}$ is large. Therefore, the LSV is created by the self-amplification of strain rate and vorticity, but is also annihilated by their self-diminution. Although the strain rate increases when $\Omega_{ik}\Omega_{kj}S_{ji} < 0$, its increase is not sufficiently large to prevent the tube from decaying at this stage. Isolated nearly axisymmetric vortex tubes have often been observed in previous studies, e.g. by Pumir (1996). These tubes are amplified for a while, but then they decay by the same mechanism. Figure 5(*b*) shows the isosurfaces of the $-S_{ij}\Pi_{ji}$ term in (2.4) near the axis of the tube shown in figure 5(*a*) in addition to those of $[A_{ij}]_+$ (grey) at $t = 1.95$. Positive and negative values of $-S_{ij}\Pi_{ji}$ are drawn using red and blue, respectively. In the left half of the tube indicated using the black arrow in figure 5(*b*), $-S_{ij}\Pi_{ji}$ is negative and contributes to a decrease in σ_s, while in the right half indicated using the white arrow, it is positive and contributes to an increase in σ_s. We consider that this non-uniform variation is due to the variation of p caused by the axial Kelvin wave propagating along the tube axis, as was pointed out in Verzicco, Jiménez & Orlandi (1995), in which it was shown that when $\sigma_s\omega_s^2 < 0$ the axial vorticity (ω_s) is rotated into a radial component (ω_+) (see § 2.6). This reorientation does not occur at the present R_λ because the magnitudes of the vorticity and strain rate are not sufficiently large at this stage (see § 4).

The start of the creation of Example I can be defined as the appearance of the recirculation flow ($t_b = 1.125$). The final stage can be characterized by the appearance of a negative $\sigma_s\omega_s^2$ in the core region ($t_e = 1.950$). The duration of these two stages, $t_c = t_e - t_b \approx 0.825$, is comparable to the eddy turnover time ($\tau_0 = 0.819$).

2.6. *Intermode transition and frequency of appearance of each mode*

Figure 14 shows the isocontours of enstrophy decomposed into components perpendicular (ω_y^2) and parallel ($\omega_x^2 + \omega_z^2$) to the page. ω_y^2 is dominant along the lower sheet and $\omega_x^2 + \omega_z^2$ is dominant along the upper sheet. Noting that the axis of the vortex tube shown in figure 5 indicated by the black arrow is nearly perpendicular to the (x, z)-plane, Example I is asymmetric and is in Mode 2 (figure 1*b*). Figure 15(*a*) shows a schematic of the arrangement of the vorticity vectors $\boldsymbol{e}_s$ and $\boldsymbol{e}_+$ along the lower (L) and upper (U) sheets and tube. On L, $\boldsymbol{e}_s$ is parallel to the tube axis and $\boldsymbol{e}_+$ is perpendicular to the axis, whereas on U, $\boldsymbol{e}_s$ is perpendicular to the axis and $\boldsymbol{e}_+$ is parallel to the axis.

The conventional rolling-up of a single vortex sheet due to the Kelvin–Helmholz instability yields only an LSV in Mode 1 because a stability analysis of the stagnation-point flow showed that a vorticity component perpendicular to the direction of the diverging flow decays (Kerr & Dold 1994), and that a parallel component can grow. This Mode 2 LSV is created due to the reorientation of the vorticity on S2 from the direction parallel to the page to that perpendicular to the page in stages [ii] and [iii].

Figure 16(*a*) shows the isocontours of $[A_{ij}]_+$ and $\sigma_s\omega_s^2$ at $t = 1.150$; $\sigma_s\omega_s^2$ is negative on L, whereas it is positive on U. In turn, the azimuthal component $\sigma_+\omega_+^2$ takes

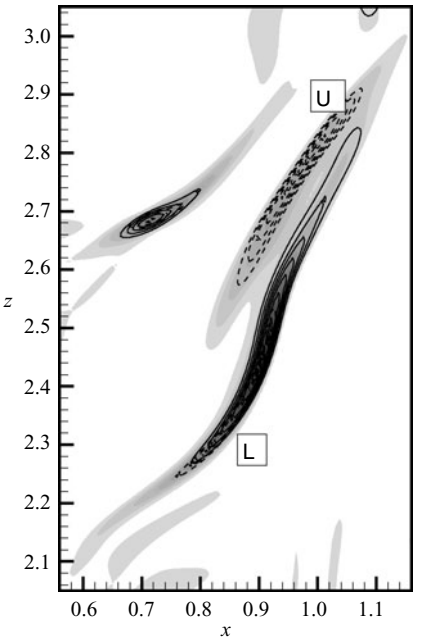

FIGURE 14. Isocontours of $[A_{ij}]_+$ [400 to 5200 (400)] and enstrophy in the (x, z)-plane at $y = 0.27$ and $t = 1.75$. The axial (ω_y^2 [2000 to 10000 (1000)]) and azimuthal components ($\omega_x^2 + \omega_z^2$ [2500 to 5500 (500)]) are plotted by solid and dashed lines, respectively.

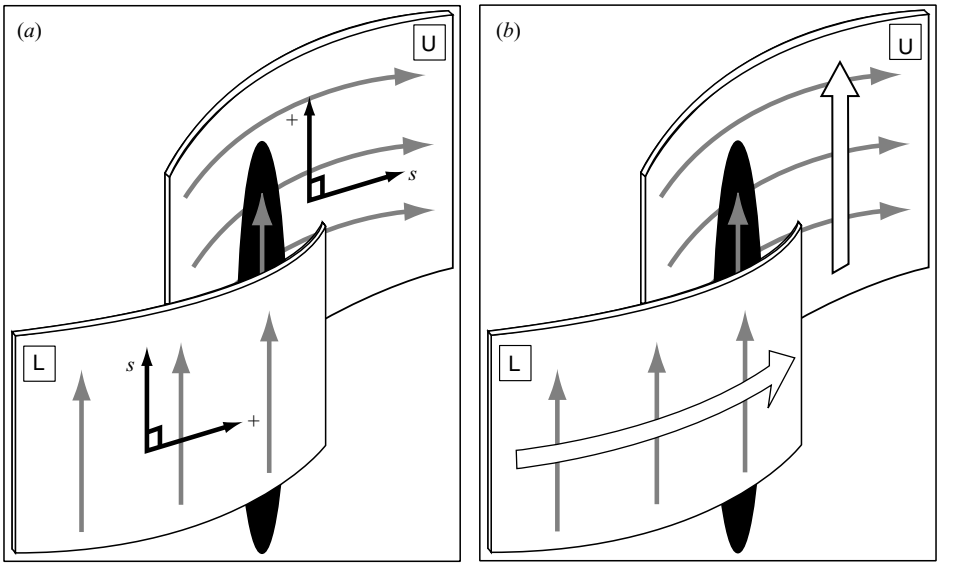

FIGURE 15. Schematic of the configuration on lower (L) and upper (U) sheets in Mode 2. Grey arrows denote vorticity vectors. (*a*) The black arrows denote the strain-rate eigenvectors $\boldsymbol{e}_s$ and $\boldsymbol{e}_+$, marked s and $+$, respectively; (*b*) the large white arrows show the velocity vectors induced by the vorticity along L and U.

large positive values in the region where $\sigma_s \omega_s^2 < 0$ on L (figure not shown). On L, ω_s^2 attenuates and ω_+^2 grows. The vorticity vectors along L are turned from the direction parallel to the page to the direction perpendicular to the page. This reorientation

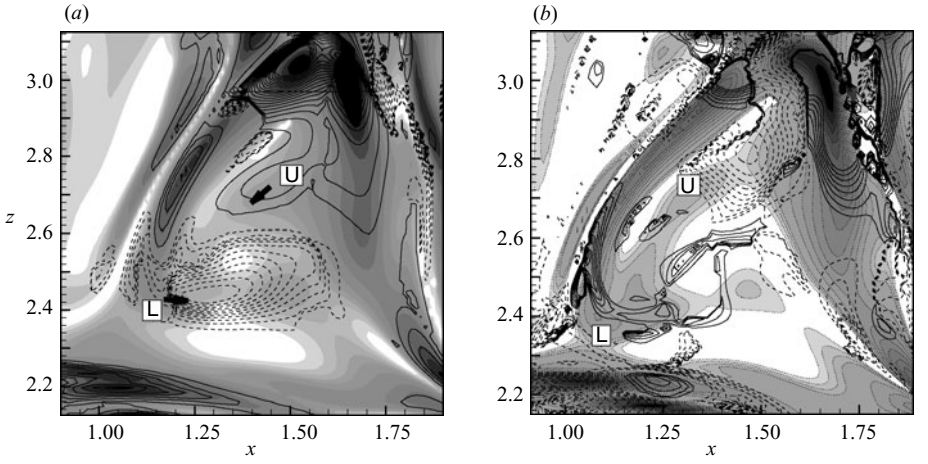

FIGURE 16. Isocontours of $[A_{ij}]_+$ (grey scale) [20 to 320] in (*a*), [50 to 600] in (*b*). The solid and dashed lines show the isocontours of (*a*) $\sigma_s\omega_s^2$ [−1100 to 10000] at $t=1.150$; and (*b*) $\widetilde{\Pi}_{ss}$ [−100 to 100] at $t=1.200$ in the (x, z)-plane at $y=0.17$. Positive values are plotted by solid lines, and negative ones by dashed lines.

does not occur on U and the vorticity direction remains parallel to the page since $\sigma_s\omega_s^2 > 0$.

The governing equations for σ_s can be derived as follows (Nomura & Post 1998):

$$\frac{\mathrm{D}}{\mathrm{D}t}\sigma_s = -\sigma_s^2 + \tfrac{1}{4}(\omega_+^2 + \omega_-^2) - \widetilde{\Pi}_{ss}, \tag{2.6}$$

where $\widetilde{\Pi}_{ij}$ is the pressure Hessian on the basis of the principal strain eigenvectors, $\boldsymbol{E}^T(\Pi_{ij})\boldsymbol{E}$. The matrices $\boldsymbol{E}$ and $\boldsymbol{E}^T$ are orthogonal and their rows and columns, respectively, are $\boldsymbol{e}_s$, $\boldsymbol{e}_+$, $\boldsymbol{e}_-$. The viscous term is omitted in (2.6). Figure 16(*b*) shows isocontours of $\widetilde{\Pi}_{ss}$ at $t=1.200$. Because $\widetilde{\Pi}_{ss}$ is positive on L, σ_s decreases with time and becomes negative, whereas $\widetilde{\Pi}_{ss}$ is negative on U and σ_s remains positive. The initial configuration is in Mode 3, but is converted into Mode 2 (Mode 3–2 transition). On L, an indefinite growth of negative σ_s is prevented by the increase in ω_+^2 (see (2.6)).

We have extracted another example of an LSV (Example II) in which a change in vorticity direction occurs on both lower and upper sheets. Figure 17 shows a schematic of the formation of Example II. Figure 18(*a*) shows the corresponding isocontours of $[A_{ij}]_+$ and the distributions of velocity vectors projected onto the (x, y)-plane. Similarly to Example I, the recirculating flow is formed through the interaction of the stagnation flow generated by S1 and S2 with S3 and the swirling flow caused by the vortex along S3. This recirculating flow concentrates and an LSV is created. Figure 18(*b*) shows the pressure Hessian term $\widetilde{\Pi}_{ss}$; is positive on both S1 and S3 in the regions indicated by the white arrows. Therefore, the vortex stretching term $\sigma_s\omega_s^2$ becomes negative on both sheets, and the initial Mode 3 configuration is converted to Mode 1 (Mode 3–1 transition). Mode 3–1 transition is akin to the expulsion of the non-axial vorticity from the tube core region shown by Pearson & Abernathy (1984), Moore (1985) and Kawahara *et al.* (1997). In Example II, $t_b \approx 0.600$, $t_e \approx 1.400$, and $t_c = t_e - t_b \approx 0.800$ which is comparable to τ_0 (=0.819) as in Example I.

Mode 3–1 and Mode 3–2 transitions can be distinguished by the swirling direction of the vortex on S3. In Mode 3–1 transition, the swirling direction is the same as that of the recirculating flow, as shown in figure 17. S3 is stretched and entrained by

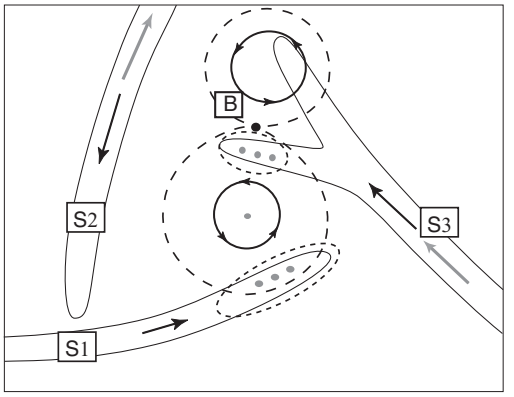

FIGURE 17. Schematic of the formation of Example II. S1, S2 and S3 are vortex sheets. The black arrows denote the velocity vector, and the grey arrows denote the vorticity vector. The long-dashed line denotes the isocontour of p, and B is the saddle point of p. The regions enclosed by the short-dashed lines are the regions in which a change in vorticity direction occurs.

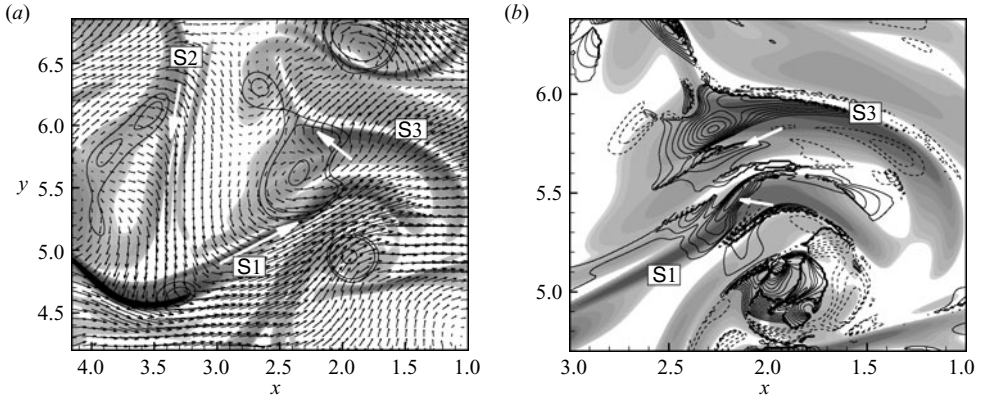

FIGURE 18. Isocontours of $[A_{ij}]_+$ (grey scale) [87.5 to 3250] in a cross-section of the (x, y)-plane at $z = 3.43$ and $t = 0.750$. The x-abscissa is reversed. (a) Distributions of velocity vectors and isocontours of p [−1.43 to −2.5]. Velocity vectors are plotted at every 6 grid points. The white arrows denote the directions of the velocity vectors on the sheets. (b) Isocontours of $\widetilde{\Pi}_{ss}$ [−60 to 80]. Positive and negative values are plotted by solid and dashed lines, respectively.

the recirculating flow. The stretched portion of S3 is placed inside the saddle point of the pressure p marked B in figure 17. As a result, the distribution of p along the stretched portion of S3 is concave as can be seen in figure 18(a), and $\widetilde{\Pi}_{ss} > 0$ as in figure 18(b). Because the distribution of p on S1 is also concave, the reorientation also occurs on S1. In Mode 3–2 transition (figure 7c), the swirling direction is opposite to that of the recirculating flow. S3 is stretched by both recirculating and swirling flows. The stretched portion of S3 is in the vicinity of the saddle point of p marked B in figure 7(c). The distribution of p along the heavy black line on the stretched portion of S3 shown in figure 8(b) is convex (see also figure 7b, d), and $\widetilde{\Pi}_{ss} < 0$ as in figure 16(b). The reorientation does not take place on S3, whereas the distribution of p is concave along S2, and the reorientation occurs on S2.

Figure 19(a) shows the p.d.f. of $\widetilde{\Pi}_{ss}$ conditionally sampled in the region in which the strain rate and vorticity are comparably large (flat sheet) (Horiuti 2001). At an

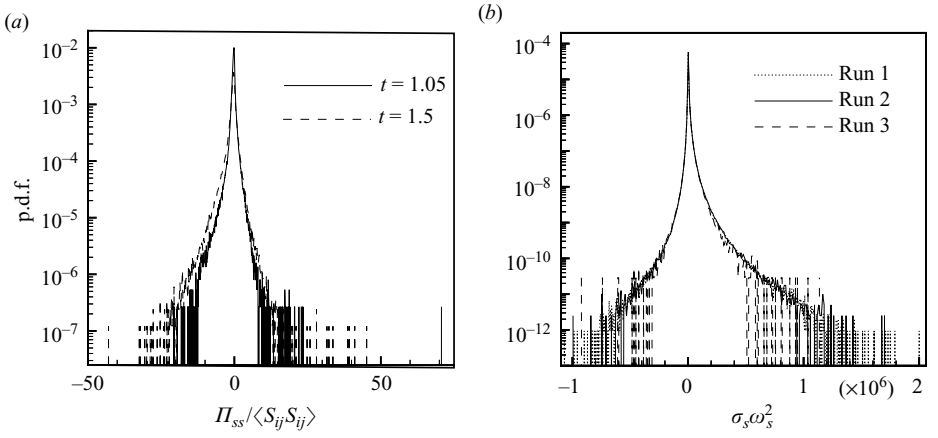

FIGURE 19. Distribution of the p.d.f. in the flat sheet region at $t = 1.900$. (*a*) $\widetilde{\Pi}_{ss}$ obtained from Run 1 (p.d.f. is plotted every 2 bins), (*b*) $\sigma_s\omega_s^2$ obtained from Runs 1–3 (every 4 bins).

early stage ($t = 1.05$), the p.d.f. is skewed to positive values, which indicates that a Mode 3–1 or 3–2 transition could occur. At a later time ($t = 1.5$), the p.d.f. becomes skewed to negative values. The conversion of the vorticity direction is complete, and the vorticity in the new direction grows.

2.7. *Persistence of each mode*

A straightforward entrainment of two vortex sheets, e.g. S2 and S3 in figure 7(*b*) and S1 and S3 in figure 18(*a*), by the recirculating flow results in a Mode 3 LSV. The formation of streamwise vortices in Mode 3 by the convergence of the recirculating flow, which is generated by the interaction of high- and low-speed streaks, has been shown in shear turbulence (Waleffe 2003). Figure 19(*b*) shows the p.d.f. for $\sigma_s\omega_s^2$ in the flat sheet region obtained from Runs 1 to 3. The large-value tails tend to become broader as the grid is refined. Because the formation of a Mode 1 LSV by rolling-up of a single sheet is associated with only positive σ_s, the appearance of a markedly large proportion of negative $\sigma_s\omega_s^2$ in figure 19(*b*) and the predominantly positive p.d.f. of $\sigma_+\omega_+^2$ (figure not shown) indicate that Mode 3–1 or 3–2 transition frequently occurs in homogeneous isotropic turbulence. As a result, a Mode 3 LSV is seldom observed in our DNS data at the later stage of development. Note that a negative $\sigma_s\omega_s^2$ also implies the occurrence of vortex compression as discussed in § 2.5, but at the annihilation stage the conversion of ω_s into ω_+ does not occur because the magnitude of ω_+ is very small.

In the Mode 2 LSV shown in figure 12, the differential rotation induced by the vortex tube and sheets is weaker along the upper sheet than along the lower sheet. Therefore, stronger stretching and a more intense energy cascade and dissipation occur along the lower sheet than along the upper sheet as can be seen in figure 13. The schematic of the distributions of the vorticity and velocity vectors in Mode 2 shown in figure 15(*b*) explains this result. The vorticity along L induces velocity azimuthal to the tube axis, while that along U induces velocity parallel to the tube axis. Therefore, more intense differential rotation is induced along L than along U.

Next, we examine Mode 2 in terms of its intercomponent energy transfer. The governing equations for the components of the energy along $\boldsymbol{e}_s$, u_s^2, and along $\boldsymbol{e}_+$, u_+^2,

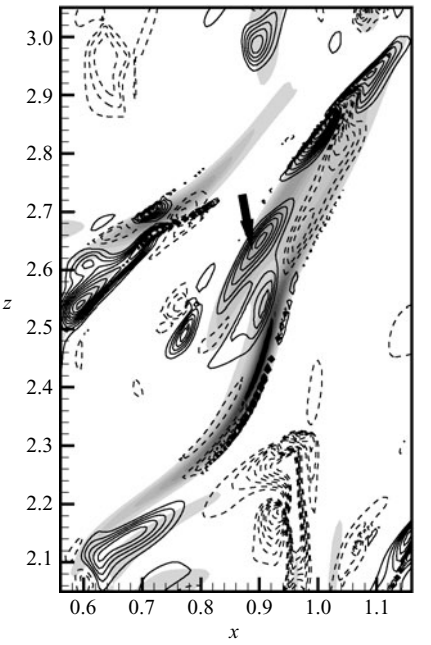

FIGURE 20. Isocontours of $[A_{ij}]_+$ (grey scale) [400 to 4800] in the (x, z)-plane at $y = 0.27$ and at $t = 1.750$ (Run 1). The solid and dashed lines show the isocontours of $-\frac{1}{4}(u_s u_+ \omega_s \omega_+)$ [−200 to 300].

are

$$\frac{\mathrm{D}}{\mathrm{D}t}\left(\frac{1}{2}u_s^2\right) = -\frac{1}{4}\frac{u_s u_+}{\sigma_s - \sigma_+}(\omega_s\omega_+ - \widetilde{\Pi}_{s+}), \tag{2.7}$$

$$\frac{\mathrm{D}}{\mathrm{D}t}\left(\frac{1}{2}u_+^2\right) = +\frac{1}{4}\frac{u_s u_+}{\sigma_s - \sigma_+}(\omega_s\omega_+ - \widetilde{\Pi}_{s+}), \tag{2.8}$$

where only relevant terms are shown. Figure 20 shows isocontours of $-\frac{1}{4}(u_s u_+ \omega_s \omega_+)$ obtained from Example I. This term is predominantly positive in the region along the upper sheet indicated by the black arrow (the contribution of $u_s u_+ \widetilde{\Pi}_{s+}$ is negligible along the upper sheet). Because $\sigma_s - \sigma_+ < 0$ along the sheet (Horiuti 2001), u_s^2 is reduced and converted to u_+^2 along the upper sheet. Similarly, the enstrophy component ω_s^2 tends to be reduced and converted to the component ω_+^2 near the upper sheet due to the action of the pressure Hessian term $\omega_s\omega_+\widetilde{\Pi}_{s+}/(\sigma_s - \sigma_+)$ (figure not shown), i.e. the vorticity direction tends to be reoriented toward the tube axis even at the later stage of development ($t = 1.750$). With regard to the intercomponent energy and enstrophy exchange, the configuration on the upper sheet of Mode 2 tends to be converted into that on the lower sheet of Mode 2, i.e. Mode 2 tends to be converted into Mode 1. A Mode 1 LSV is more persistent than a Mode 2 LSV. The effect of the upper sheet in a Mode 2 LSV is not critically important in the turbulence cascade. The same would be true for the Mode 3 LSV. In fact, the slope of the energy spectrum which a Mode 3 LSV induces is −7/3 (Pullin & Lundgren 2001). The slope induced by a Mode 2 LSV is intermediate between −5/3 and −7/3. In Kawahara *et al.* (1997), it was shown that as the spiral turns tighten, the azimuthal vorticity in the neighbouring spiral

sheets induces axial shear flows which tilt the vorticity toward the axial direction. The conversion of Mode 2 to Mode 1 may be related to this mechanism.

It is difficult to quantify the percentage of LSVs in Mode 1 or 2 (or Mode 3). Since the probability of the swirling direction of the vortex along S3 being clockwise or counterclockwise is considered to be even, Mode 3–1 or 3–2 transition may occur nearly equally. Along the vortex tube in Example II, the reorientation of the vorticity direction takes place on two sheets for some cross-sections, but occasionally it takes place only on one of the two sheets in another cross-section. In general, it appears that the LSV is in a mixture of Mode 1 and 2 configurations. The non-uniformity of the mode along the vortex tube may lead to the formation of the helical structures observed in previous studies, e.g. Vincent & Meneguzzi (1994).

In figure 5, the vortex tube marked by the white arrow is in Mode 1, whereas that marked by the black arrow (Example I) is in Mode 2. It is interesting to note that these two tubes are nearly transversely aligned. The Mode 2 LSV occasionally yields this configuration, but it was shown by Holm & Kerr (2002) that this helical state is associated with a vorticity surge.

3. Estimate of the thickness of the spiral sheet

As shown in § 2, the spiral sheet is stretched to a very small thickness. In this section, we estimate the average thickness of the vortex sheet by fitting the computed energy spectrum, $E(k, t)$, with the assumed functional form:

$$E(k, t) = c(t)k^{-n(t)}\mathrm{e}^{-2\delta(t)k}, \tag{3.1}$$

where $\delta(t)$ is the logarithmic decrement and $n(t)$ is the algebraic prefactor (Brachet *et al.* 1992). The validity of this fitting is assessed in figure 4, which includes the profile of the energy spectrum estimated using (3.1) in Run 1. The fitted spectrum coincides with the exact spectrum in the range $k\overline{\eta} \geqslant 0.1$. In (3.1), $\delta(t)$ provides an estimate of the average thickness of the vortex sheet (Sulem, Sulem & Frisch 1983).

Figure 21 shows the temporal evolutions of $\delta(t)$ normalized by $\overline{\eta}(t)$ obtained from Runs 1–3. At early time, $\delta(t)$ exhibits an almost inviscid exponential decay followed by a slowing down due to viscosity, and after reaching its minimum, $\delta(t)$ converges to its asymptotic value (Passot *et al.* 1995). When the fitting is carried out using the wavenumber range of $k = 5$–$k_{\max}$, the three runs show marked differences. The asymptotic thickness of the sheet from Run 1 ($\approx 2.05\ \overline{\eta}$) is smaller than those from Runs 2 ($\approx 2.34\ \overline{\eta}$) and 3 ($\approx 3.21\ \overline{\eta}$). In figure 11, the size of the computational grid cell is shown for reference using a black square placed at $x \approx 1.0, z \approx 2.15$. The estimate of the thickness obtained using this grid cell agrees approximately with the estimate obtained using (3.1) (the grid interval Δ is $0.78\ \overline{\eta}$ in Run 1). Because the fittings using the range of $k = 5$–255 (denoted as 1024 ($k = 5$–255) in the figure) and $k = 5$–127 (1024 ($k = 5$–127)) using the data from Run 1 yield evolutions similar to those obtained from Runs 2 and 3, respectively, the fine-scale structure of the LSV is not fully resolved in Runs 2 and 3, as noted in § 2.1.

The extraction of fine dissipative structures of an LSV is markedly affected by grid resolution. The results obtained from Run 3 ($k_{\max}\overline{\eta} \approx 1.0$) which corresponds to those obtained from Run 1 (figure 11) are shown in figure 6 of Horiuti & Takagi (2005). The contours of the vortex sheet were fragmented, and spiral turns were indistinct and not well captured, although the vortex tubes were fully resolved. In Run 2 ($k_{\max}\overline{\eta} \approx 2.0$), the spiral turns of the vortex sheets are distinct but the contours of the sheets are still fragmented, which is pronounced at $t \gtrsim 1.7$ (figure not shown). In Run 1 ($k_{\max}\overline{\eta} \approx 4.0$),

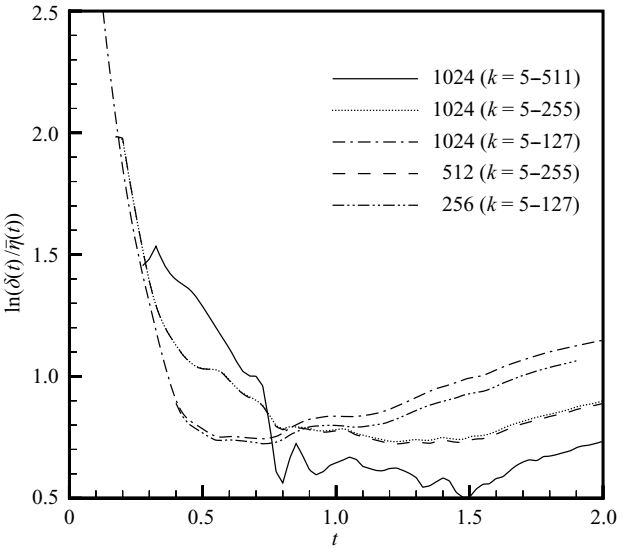

FIGURE 21. Temporal evolution of logarithmic decrement $\delta(t)$ normalized by $\overline{\eta}(t)$ obtained from Run 1 (denoted as 1024), 2 (512), 3 (256).

this fragmentation is eliminated as was shown for the scalar field by Schumacher, Sreenivasan & Yeung (2005). Note that no additional numerical smoothing is applied to the contours. These results indicate that a very high resolution of the vortex sheet is required to accurately capture the LSV. We believe that the spiral structures were not observed by Ruetsh & Maxey (1992), Vincent & Meneguzzi (1994) and Pumir (1996) partly because $k_{\max}\overline{\eta} \approx 1.0-2.0$ in their data. We note that even the contours obtained from Run 1 still exhibit a weak fragmentation in figure 11. Moreover, $\delta(t)$ shown in figure 21 exhibits no apparent tendency of convergence as the grid is refined. Even the resolution of $k_{\max}\overline{\eta} \approx 4.0$ may be insufficient to resolve the very fine scales of the LSV. In fact, $\eta_{\min}/\Delta \approx 0.41$ in Run 1 (≈ 0.20 and 0.11 in Runs 1 and 2, respectively) at $t = 2.0$, where $\eta_{\min}$ denotes the minimum of the local Kolmogorov scale η $(=\nu^{3/4}/\varepsilon^{1/4})$ in the whole domain. The requirement for substantially better resolution to study the properties of sub-Kolmogorov scales was pointed out in Jiménez & Wray (1998). The estimate of required grid points number for DNS deduced in Sreenivasan (2004), $N \propto R_\lambda^2$, appears to be more reasonable than the conventional estimate of $N \propto R_\lambda^{3/2}$.

4. LSV formation at higher Reynolds number

In this section, we investigate the effect of the Reynolds number on the structure of an LSV using Run 4. Figure 22 shows the distributions of $[A_{ij}]_+$ and p at $t = 1.950$ obtained from Run 4, which exhibit a marked difference from those obtained from Run 1 (see figure 11). The stretched vortex sheets emanating from the core region of the LSV are thinner, and the spiral has more turns due to the more intense differential rotation. At higher Reynolds numbers, the spiral rotates and wraps continuously around itself into ever tighter coils. This LSV entrains many of the sheets surrounding its core region in addition to the sheets marked L and U in figure 9(*b*), e.g. the sheets marked SA, SB and SC.

Another notable feature of Run 4 is the creation of extra LSVs, e.g. the LSV along the upper sheet in the region indicated by the black arrow in figure 22. At low

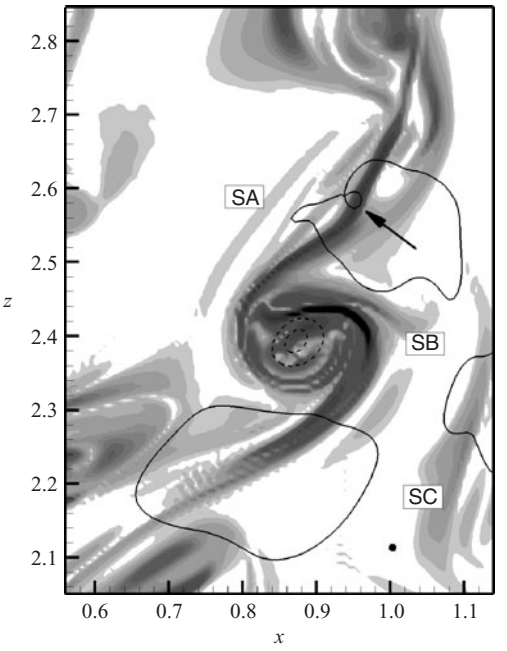

FIGURE 22. Isocontours of $[A_{ij}]_+$ (grey scale) [150 to 17500] obtained from Run 4. The solid and dashed lines show the isocontours of p [−9.0, −7.0, 0.21] in the (x, z)-plane at $y = 0.17$ and $t = 1.950$. Positive values are plotted by solid lines, and negative ones by dashed lines.

Reynolds numbers, the LSV in Run 1 shown in figure 11 gradually fades due to the vortex compression and viscous effect, and this extra LSV is not created. In a linear stability analysis for a Burgers vortex layer (Beronov & Kida 1996), it was shown that the layer is unstable when $Re_l = U_0/\sqrt{A\nu} \geqslant 1$, where A and U_0 are the strength of the stagnation-point flow and strain, respectively. Noting that $Re_l \approx 1.25(\Omega_B(0)/A)$ ($\Omega_B(0)$ denotes the vorticity of the layer), the layer vorticity and Re_l increases in Run 4 because the velocity difference across the layer is preserved but the layer becomes thinner by stretching. The newly created LSV indicated by the black arrow in figure 22 rolls up and grows with time as shown in figure 23 at $t = 2.125$. The formation of other LSVs can be seen in figure 23, e.g. the one marked by the black arrow at $x = 1.05$, $z = 2.23$. These newly created LSVs again stretch the vortex sheet emanating from them, and also entrain other sheets surrounding them by differential rotation. Note that the spiral sheets in the core region of Example I also roll up and many small-scale LSVs are created in the core region.

Although we show only two examples, Examples I and II, there are many regions in figure 6 similar to the region marked by the heavy dashed line, in which the two sheets intersect nearly perpendicularly and the recirculating flow represented by the red circles resides in the vicinity of the two sheets. Therefore, many LSVs similar to Examples I and II are created. The maximum values of ω_i^2 in Examples I and II are $40.5\langle\omega_i^2\rangle$ (at $t = 1.95$) and $27.3\langle\omega_i^2\rangle$ (at $t = 1.0$), respectively. Both examples are strong vortices (Jiménez & Wray 1998). These LSVs, which are created by an interaction among several sheets, tend to possess a large vorticity because the large circulation in the recirculating region is confined to the core region of the LSV with a small cross-section area (primary instability). These LSVs are long in the lateral direction, e.g. the length of the vortex tube in Example I is 0.65 ($\approx 1.40\,L$) (figure 5). These constitute

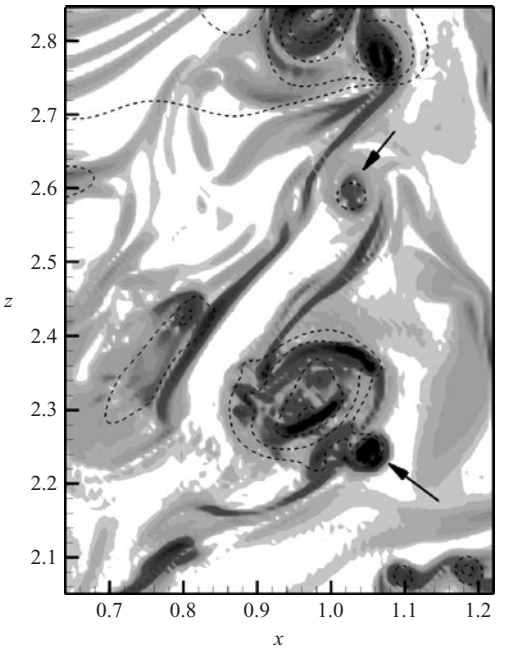

FIGURE 23. Isocontours of $[A_{ij}]_+$ (grey scale) [150 to 12500] obtained from Run 4. The dashed lines show the isocontours of p [−8.0 to −1.0] in $x-z$ plane at $y=0.17$ and $t=2.125$.

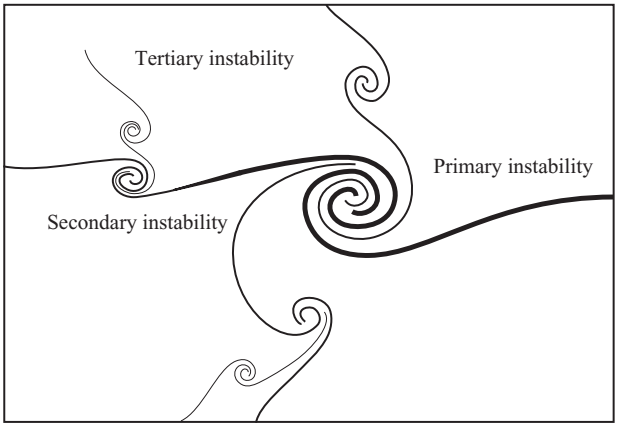

FIGURE 24. Schematic of network of hierarchical LSVs created by the instability cascade.

the LSVs on the largest scale. They stretch the spiral arms emanating from them, and the stretching induces the instability of the spiral arms and leads to the creation of the second generation of LSVs (secondary instability). Then, the second generation of LSVs strains and stretches the vorticity blobs in their neighbourhood. With the stretching of these blobs, tertiary instability is induced, and the third generation of LSVs is created by rolling-up of the stretched blobs. As the cascade progresses, the instability creates an LSV carrying smaller circulation. This instability cascade (Jiménez & Wray 1998) is schematically shown in figure 24.

Extending this argument, this process would be repeated until the scale reaches a minimum imposed by molecular diffusion. High Reynolds numbers would lead to the formation of hierarchical cluster of self-similar LSV networks, and induce the cascade of energy to small scales. Because the lateral extent of the cluster is several times larger than the integral-length scale L, LSVs with an extensive range of scales are contained in the cluster. As a result, the energy spectrum obtained from Run 4 shown in figure 4 approximately fits the Kolmogorov $-5/3$ law for about a decade, and the enstrophy (or the dissipation rate) increases very rapidly in Run 4 (figure 2*b*). A similar cascade model was considered by Childress (1984), in which self-similar eddies were created by splitting of tubes. Although a spiral with a large number of turns is folded at many self-similar scales (Lundgren 1993), the spiral itself may not induce the fractal nature of the dissipation field, but hierarchical LSVs would cause such fractality. Note that small-scale LSVs may be dominant in Mode 1 because they are formed primarily by rolling-up of a stretched vortex sheet. This Mode 1 LSV induces the $-5/3$ energy spectrum (Lundgren 1982).

The spiral turns of very thin sheets and the creation of hierarchical LSVs at high R_λ cause a strong intermittency of the small scale and dissipation field because LSVs are created in small subsets of the flow field instead of space-filling subsets. It is generally considered that the normalized dissipation rate $\langle\varepsilon\rangle L/u'^3$ tends to a non-zero constant as $\nu \to 0$ (Sreenivasan 1998). To accomplish this convergence, the velocity derivatives should diverge as $\nu \to 0$. This divergence may be attributed to the thinning of the spiral sheet to extreme length induced by hierarchical LSVs. As a common drawback of the run with $k_{\max}\overline{\eta} \approx 1.0$ noted in § 3, the contours of the vortex sheets shown in figure 23 exhibit serious fragmentation, and very thin blobs stretched by small-scale LSVs are not captured. A study using higher resolution is underway.

5. Conclusions

We have identified a stretched spiral vortex (Lundgren 1982, LSV) using DNS data for homogeneous isotropic turbulence, and its properties have been presented. Its genesis, growth and annihilation are elucidated, and the roles of the LSV in the generation of turbulence are shown. Besides the two symmetric configuration modes studied in previous works, in which a vortex sheet whose vorticity is either parallel (Mode 1) or perpendicular (Mode 3) to a vortex tube is wrapped into a spiral, a third asymmetric mode (Mode 2) is identified, in which one branch of the spiral has vorticity parallel to the tube, and that of the other is perpendicular to the tube. A conventional rolling-up of a single vortex sheet yields a Mode 1 LSV. Mode 2 and 3 LSVs are created not by this rolling-up but through the interaction of several sheets. The stagnation flow caused by two sheets converges to form the recirculating flow by an interaction with the vortex along the third sheet. This recirculating flow strains and stretches the sheets. A vortex tube is formed by axial straining provided by the other vortices, the lowering of pressure and the intensification of the swirling motion in the recirculating region. By the differential rotation induced by the tube and that self-induced by the sheet, the vortex sheets are entrained by the tube and form spiral turns. The initial configuration is Mode 3, which is transformed into either Mode 1 or 2. This transformation is due to the compression of one of the pre-existing sheets before being wrapped, in such a way that its azimuthal vorticity is damped, and its axial vorticity is amplified. On at least one of the two sheets, the compression of azimuthal vorticity usually occurs by the action of the pressure Hessian term. On another sheet, compression occurs when the vortex on the third sheet swirls in

the same direction as that in the recirculating flow. Mode 1 and Mode 2 LSVs are considered to be created almost equally, but Mode 1 tends to be more persistent than Mode 2.

By tightening of the spiral turns, spiral sheets are stretched to extreme lengths. The cascade of velocity fluctuations to smaller scale and more intense dissipation take place along spiral sheets (Lundgren 1982). The local dissipation rate ε and Kolmogorov scale η exhibit a strong intermittency (Schumacher *et al.* 2005). It is shown that a grid resolution with at least $k_{\max}\overline{\eta} \approx 4.0$ is indispensable for a precise capture of the spiral turns and dissipation field at $R_\lambda \approx 80$.

At a higher Reynolds number, the hierarchical cluster of spiral vortices is formed due to the instability cascade induced by the stretching of vortex sheets. As the cascade progresses, self-similar LSVs carrying smaller circulations are successively created. The lateral extent of this cluster is several times the integral scale, and this LSV cluster comprises an entire range of length scales from the overall scale of the structure to a minimal Kolmogorov scale. As a result, this cluster induces an energy cascade and the energy spectrum fits the Kolmogorov $-5/3$ law.

We are grateful for the valuable comments from anonymous referees, and also to Y. Takagi for valuable discussions and K. Saito for providing the DNS data for Run 4 and figures 5 and 6. This work is partially supported by Grants-in-Aid from the Ministry of Education, Culture, Sports, Science and Technology, Japan (Nos. 16560136 and 18560156). Main computations are performed at National Institute for Fusion Science, Cybermedia Centre, Osaka University, and Information Synergy Centre, Tohoku University.

REFERENCES

Andreotti, B. 1997 Studying Burgers' models to investigate the physical meaning of the alignments statistically observed in turbulence. *Phys. Fluids* **9**, 735–742.

Beronov, K. N. & Kida, S. 1996 Linear two-dimensional stability of a Burgers vortex layer. *Phys. Fluids* **8**, 1024–1035.

Brachet, M. E., Meneguzzi, M., Vincent, A., Politano, H. & Sulem, P. L. 1992 Numerical evidence of smooth self-similar dynamics and possibility of subsequent collapse for three-dimensional ideal flows. *Phys. Fluids* A **4**, 2845–2854.

Burgers, J. M. 1948 A mathematical model illustrating the theory of turbulence. *Adv. Appl. Mech.* **1**, 171.

Chasnov, J. R. 1991 Simulation of the Kolmogorov inertial subrange using an improved subgrid model. *Phys. Fluids* A **3**, 188–200.

Childress, S. 1984 A vortex-tube model of eddies in the inertial range. *Geophys. Astrophys. Fluid Dyn.* **29**, 29–64.

Dávila, J. & Vassilicos, J. C. 2003 Richardson's pair diffusion and the stagnation point structure of turbulence. *Phys. Rev. Lett.* **91**, 144501.

Gilbert, A. D. 1993 A cascade interpretation of Lundgren's stretched spiral vortex model for turbulent fine structure. *Phys. Fluids* A **5**, 2831–2834.

Herring, J. R. & Kerr, R. M. 1993 Development of enstrophy and spectra in numerical turbulence. *Phys. Fluids* A **5**, 2792–2798.

Holm, D. D. & Kerr, R. M. 2002 Transient vortex events in the initial value problem for turbulence. *Phys. Rev. Lett.* **88**, 244501.

Horiuti, K. 2001 A classification method for vortex sheet and tube structures in turbulent flows. *Phys. Fluids* **13**, 3756–3774.

Horiuti, K. 2003 Roles of nonaligned eigenvectors of strain-rate and subgrid-scale stress tensors in turbulence generation. *J. Fluid Mech.* **491**, 65–100.

Horiuti, K. & Takagi, Y. 2005 Identification method for vortex sheet structures in turbulent flows. *Phys. Fluids* **17**, 121703.

Jiménez, J. & Wray, A. A. 1998 On the characteristics of vortex filaments in isotropic turbulence. *J. Fluid Mech.* **373**, 255–285.

Kawahara, G. 2005 Energy dissipation in spiral vortex layers wrapped around a straight vortex tube. *Phys. Fluids* **17**, 055111.

Kawahara, G., Kida, S., Tanaka, M. & Yanase, S. 1997 Wrap, tilt and stretch of vorticity lines around a strong thin straight vortex tube in a simple shear flow. *J. Fluid Mech.* **353**, 115–162.

Kerr, R. M. 1985 Higher-order derivative correlations and the alignment of small-scale structures in isotropic numerical turbulence. *J. Fluid Mech.* **153**, 31–325.

Kerr, O. S. & Dold, J. W. 1994 Periodic steady vortices in a stagnation-point flow. *J. Fluid Mech.* **491**, 307–325.

Kida, S. & Miura, H. 1998 Identification and analysis of vortical structures *Eur. J. Mech.* B/*Fluids* **17**, 471–488.

Kida, S. & Miura, H. 2000 Double spirals around a tubular vortex in turbulence. *J. Phys. Soc. Japan* **69**, 3466–3467.

Lundgren, T. S. 1982 Strained spiral vortex model for turbulent structures. *Phys. Fluids* **25**, 2193–2203.

Lundgren, T. S. 1993 A small-scale turbulence model. *Phys. Fluids* A **5**, 1472–1483.

Lundgren, T. S. & Mansour, N. N. 1996 Transition to turbulence in an elliptic vortex. *J. Fluid Mech.* **307**, 43–62.

Malik, N. A. & Vassilicos, J. C. 1996 Eulerian and Lagrangian scaling properties of randomly advected vortex tubes. *J. Fluid Mech.* **326**, 417–436.

Moore, D. W. 1985 The interaction of a diffusing vortex and an aligned shear flow. *Proc. R. Soc. Lond.* A **399**, 367–375.

Neu, J. C. 1984 The dynamics of stretched vortices. *J. Fluid Mech.* **143**, 253–276.

Nomura, K. K. & Post, G. K. 1998 The structure and dynamics of vorticity and rate of strain in incompressible homogeneous turbulence. *J. Fluid Mech.* **377**, 65–97.

Passot, T., Politano, H., Sulem, P.-L. & Meneguzzi, M. 1995 Instability of strained vortex layers and vortex tube formation in homogeneous turbulence. *J. Fluid Mech.* **282**, 313–338.

Pearson, C. F. & Abernathy, F. H. 1984 Evolution of the flow field associated with a streamwise diffusing vortex. *J. Fluid Mech.* **146**, 271–283.

Pullin, D. I. & Lundgren, T. S. 2001 Axial motion and scalar transport in stretched spiral vortices. *Phys. Fluids* **13**, 2553–2563.

Pumir, A. 1996 A numerical study of pressure fluctuations in three-dimensional, incompressible, homogeneous, isotropic turbulence. *Phys. Fluids* **6**, 2071–2083.

Rosales, C. & Meneveau, C. 2006 A minimal multiscale Lagrangian map approach to systhesize non-Gaussian turbulent vector fields. *Phys. Fluids* **18**, 075104.

Ruetsh, G. R. & Maxey, M. R. 1992 The evolution of small-scale structures in homogeneous turbulence. *Phys. Fluids* A **4**, 2747–2760.

Schumacher, J., Sreenivasan, K. R. & Yeung, P. K. 2005 Very fine structures in scalar mixing. *J. Fluid Mech.* **531**, 113–122.

Sreenivasan, K. R. 1998 An update on the energy dissipation rate in isotropic turbulence. *Phys. Fluids* **10**, 528–529.

Sreenivasan, K. R. 2004 Possible effects of small-scale intermittency in turbulent reacting flows. *Flow, Turbulence Combust.* **72**, 115–131.

Sulem, C., Sulem, P. L. & Frisch, H. 1983 Tracing complex singularities with spectral methods. *J. Comput Phys.* **50**, 138–161.

Verzicco, R., Jiménez, J. & Orlandi, P. 1995 On steady columnar vortices under local compression. *J. Fluid Mech.* **299**, 367–388.

Vincent, A. & Meneguzzi, M. 1994 The dynamics of vorticity tubes in homogeneous turbulence. *J. Fluid Mech.* **258**, 245–254.

Waleffe, F. 2003 Homotopy of exact coherent structures in plane shear flows. *Phys. Fluids* **15**, 1517–1534.